

CHEBYSHEV SPECTRAL METHODS  
*with applications to*  
ASTROPHYSICAL FLUID DYNAMICS

KEATON J. BURNS

May 3, 2013

**Contents**

<b>1</b>	<b>Introduction</b>	<b>2</b>
<b>2</b>	<b>Theory of spectral methods</b>	<b>2</b>
2.1	Series convergence . . . . .	2
2.2	Fourier series . . . . .	3
2.3	Chebyshev series . . . . .	5
2.4	Galerkin method . . . . .	7
2.5	Pseudospectral method . . . . .	8
<b>3</b>	<b>Solving linear ordinary differential equations</b>	<b>10</b>
3.1	Selecting a grid . . . . .	10
3.2	Constructing the pseudospectral matrices . . . . .	11
3.3	Generalized eigenvalue equations . . . . .	13
3.4	Implementing boundary conditions . . . . .	14
3.5	Solving systems of equations . . . . .	15
<b>4</b>	<b>ODE Examples</b>	<b>16</b>
4.1	Plucked string . . . . .	16
4.2	Stratified magnetorotational instability . . . . .	17
4.3	Plane-parallel heat-flux buoyancy instability . . . . .	20
<b>5</b>	<b>Solving partial differential equations</b>	<b>21</b>
5.1	Constructing the time derivative . . . . .	22
5.2	Explicit time marching . . . . .	23
5.3	Modified grids . . . . .	24
5.4	Implementing boundary conditions . . . . .	26
<b>6</b>	<b>PDE Examples</b>	<b>28</b>
6.1	Wave equation . . . . .	28
6.2	Kuramoto-Sivashinsky equation . . . . .	30
6.3	Complex Ginzburg-Landau equation . . . . .	31
<b>7</b>	<b>Conclusion</b>	<b>34</b>

# 1 Introduction

A spectral method is a general approach to numerically solving a differential equation by assuming that a good approximate solution can be constructed as the sum of a finite set of basis functions. Knowing how to differentiate the basis elements allows one to determine the combination of basis functions that best satisfies the differential equation, a process which becomes exponentially more accurate as additional terms are added. While there are many useful sets of basis functions, we will focus on Chebyshev polynomials. These orthogonal polynomials are related to the Fourier series via a simple change of variables, a fact which allows much of the theory and many of the computational tools developed for Fourier series to be applied to finite domains through the Chebyshev polynomials.

Section 2 develops the convergence properties of Fourier and Chebyshev series, allowing us to estimate the error in approximating a given function by a finite number of sinusoids or Chebyshev polynomials. We then discuss the two main types of spectral methods: the integration and interpolation approaches. The *Galerkin* formulation determines the spectral coefficients of the solution by projecting terms in the differential equation against individual basis functions. An approximately equivalent formulation is the *pseudospectral* method, which instead enforces the differential equation over a set of interpolation points.

Section 3 explicitly outlines the machinery needed to numerically implement Chebyshev spectral algorithms and solve linear ordinary differential equations. Section 4 uses our open-source Python implementation of these tools to solve three eigenvalue problems: determining the eigenfrequencies of a plucked string, the normal modes of the magnetorotational instability in a stratified disc, and the normal modes of the heat-flux buoyancy instability in cool galaxy cluster cores.

Section 5 extends our framework to cover general partial differential equations with one spatial and one temporal dimension. This involves a brief discussion of explicit time-marching methods and different approaches to implementing boundary conditions. Finally, these tools are used in Section 6 to examine the wave equation with various boundary conditions, the 4-th order Kuramoto-Sivashinsky equation, and the complex Ginzburg-Landau equation.

## 2 Theory of spectral methods

We begin our analysis of Chebyshev spectral methods by defining the orders of convergence for a general spectral series. We then state several theorems on the converge of Fourier series which underpin the proofs of Chebyshev convergence. Finally, the formulations and accuracies of the Galerkin and pseudospectral methods are discussed.

This section follows the presentation offered in chapters 2-4 of [Boyd \(2000\)](#), but the definitions and theorems are common throughout the literature on spectral methods.

### 2.1 Series convergence

Consider a general series expansion of a function  $f(x)$  over a set of normalized basis functions  $\{\phi_i\}$ :

$$f(x) = \sum_{n=0}^{\infty} \alpha_n \phi_n(x) \tag{1}$$

The *asymptotic order of convergence* of such a series tells us how the coefficients  $\alpha_n$  scale for large  $n$ . For simplicity, the following definitions ignore subdominant terms that may appear in the scalings, such as logarithms when multiplied by algebraic terms, or algebraic terms when multiplied by exponentials.

**Definition:** If the coefficients of a series behave like

$$\alpha_n \sim \mathcal{O}(n^{-k}) \quad (2)$$

for large  $n$ , then  $k$  is the *algebraic index of convergence* of the series.

**Definition:** If the coefficients of a series behave like

$$\alpha_n \sim \mathcal{O}(\exp(-cn^r)) \quad (3)$$

for large  $n$  and some constant  $c$ , then the series exhibits *exponential convergence*, and  $r$  is the *exponential index of convergence*.

**Definition:** Let

$$\mu = \limsup_{n \rightarrow \infty} \log(|\alpha_n|)/n \quad (4)$$

If  $\mu = 0$ , then the series exhibits *subgeometric convergence*. If  $\mu = \infty$ , then the series exhibits *supergeometric convergence*. If  $\mu$  is a constant, then the series exhibits *geometric convergence* and  $\mu$  is the *asymptotic rate of geometric convergence* of the series.

Knowing the order of convergence of a series provides insight into the errors made by spectral methods, which in general aim to determine the first  $N + 1$  coefficients in the series expansion of the solution of a differential equation. The true solution can be expanded as

$$u(x) = \sum_{n=0}^{\infty} A_n \phi_n(x) \quad (5)$$

and the approximate solution, as provided by the spectral method, as

$$u_N(x) = \sum_{n=0}^N \alpha_n \phi_n(x) \quad (6)$$

The *truncation error* of this approximation is the error associated with neglecting terms with  $n > N$ , and, as we will see, can be estimated using the convergence properties of Fourier and Chebyshev series. The *discretization error* is the difference between the approximated coefficients  $\alpha_n$  and the true coefficients  $A_n$  for  $n = 0, \dots, N$ . Although it cannot be proven when the true solution is unknown, it is commonly assumed that the discretization error is of the same order as the truncation error, allowing the use of the latter for estimating the total error in the approximate solution.

## 2.2 Fourier series

The Fourier series of a function  $f(x)$ , written in complex form, is

$$f(x) = \sum_{n=-\infty}^{\infty} c_n \exp(inx) \quad (7)$$

$$c_n = \frac{1}{2\pi} \int_{-\pi}^{\pi} f(x) \exp(-inx) dx \quad (8)$$

Integrating Equation (8) by parts  $J + 1$  times yields

$$c_n = \frac{1}{2\pi} \sum_{j=0}^J (-1)^{n+1} \left(\frac{1}{in}\right)^{j+1} [f^{(j)}(\pi) - f^{(j)}(-\pi)] + \frac{1}{2\pi} \left(\frac{1}{in}\right)^{J+1} \int_{-\pi}^{\pi} f^{(J+1)}(x) \exp(-inx) dx \quad (9)$$

where superscripts in parentheses indicate derivatives. The integral has an upper bound of

$$2\pi \max_x |f^{(J+1)}(x)| \quad (10)$$

so as  $n \rightarrow \infty$  for fixed  $J$ , the second term behaves like  $\mathcal{O}(n^{-(J+1)})$ , yielding the Fourier asymptotic coefficient expansion:

$$c_n \sim \frac{1}{2\pi} \sum_{j=0}^J (-1)^{n+1} \left(\frac{1}{in}\right)^{j+1} [f^{(j)}(\pi) - f^{(j)}(-\pi)] + \mathcal{O}(n^{-(J+1)}) \quad (11)$$

**Theorem:** If  $f^{(i)}(\pi) = f^{(i)}(-\pi)$  and  $f^{(i)}(x)$  is continuous for  $i = 0, \dots, k - 2$ , and  $f^{(k)}$  is integrable, then the coefficients of the Fourier series of  $f(x)$  are bounded from above like

$$|c_n| \leq C|n|^{-k} \quad (12)$$

for some constant  $C$ .

The proof of the theorem follows from the coefficient expansion above with  $J = k - 1$ . This is a very useful result: the number of continuous, periodic derivatives of a function provides a lower bound on the algebraic index of convergence of that function's Fourier series. In particular, if a function is periodic and smooth (infinitely differentiable), then the series converges faster than any power of  $n$ , i.e. the series exhibits exponential convergence.

The domain and rate of convergence of the Fourier series of a function  $f(z)$  depends on the location of the singularities of  $f$  in the complex plane.

**Theorem:** Let  $\{z_j = x_j + iy_j\}$  denote the set of singularities of a function  $f(z)$ . If  $\rho$  is the magnitude of the imaginary part of the singularity that lies closest to the real axis,

$$\rho = \min_j |y_j| \quad (13)$$

then the domain of convergence of the Fourier series of  $f(z)$  is the strip centered around the real axis with width  $2\rho$ :

$$\{z = x + iy : |y| < \rho\} \quad (14)$$

and the asymptotic rate of convergence for real  $z$  is  $\mu = \rho$ . Series with a finite algebraic index of convergence have  $\rho = 0$  and only converge on the real line. Periodic and entire functions (i.e. with no singularities except possibly at  $\infty$ ) usually have  $\rho = \infty$  and converge supergeometrically.

We provide the same heuristic proof as [Boyd](#). It is clear from the form of the complex Fourier series

$$f(z) = \sum_{n=-\infty}^{\infty} c_n \exp(inz) = \sum_{n=-\infty}^{\infty} c_n \exp(inx) \exp(-ny) \quad (15)$$

that terms with negative  $n$  grow exponentially in the upper half-plane while terms with positive  $n$  grow exponentially in the lower half-plane. Therefore, the coefficients  $|c_n|$  must decay at least as fast as  $\exp(-|n|\rho)$  for the series to converge at  $|y| = \rho$ . However, since the series must converge to higher and higher values as  $z$  approaches the singularity, the coefficients cannot decay faster than, and therefore must decay like,  $\exp(-|n|\rho)$ .

Knowledge of the convergence of a Fourier series allows us to estimate the error in truncated the series after  $N$  terms. Since the Fourier basis functions are unit-normalized, the truncation error is bounded from above by the sum of the magnitudes of the neglected coefficients:

$$f_N(x) = \sum_{n=-N}^N c_n \exp(inz) \quad (16)$$

$$\Rightarrow E_T(N) = |f(x) - f_N(x)| \leq \sum_{|n|>N} |c_n| \quad (17)$$

For geometrically converging series, which have coefficients like  $c_n \sim \mathcal{O}(\exp(-\mu n))$ , this sum yields

$$E_T(N) \sim \mathcal{O}(\exp(-\mu N)) \sim \mathcal{O}(|c_N|) \quad (18)$$

while for algebraically converging series, which have coefficients like  $c_n \sim \mathcal{O}(n^{-k})$ , it yields

$$E_T(N) \sim \mathcal{O}(1/N^{k+1}) \sim \mathcal{O}(N|c_N|) \quad (19)$$

In both cases, we see that the truncation error is related to the last coefficient retained in the truncated series, providing a quick way to check whether more terms are needed to attain a given accuracy.

### 2.3 Chebyshev series

The Chebyshev polynomials of the first kind are defined by

$$T_n(x) = \cos(n\theta) \quad (20)$$

where  $\theta = \arccos(x)$ . This mapping has a simple geometric interpretation: the  $n$ -th Chebyshev polynomial is the projection onto a plane of the function  $y = \cos(n\theta)$  drawn on a cylinder, as demonstrated in Figure 1.

By inspection, we see that the first two Chebyshev polynomials are

$$T_0(x) = \cos(0) = 1 \quad (21)$$

$$T_1(x) = \cos(\arccos(x)) = x \quad (22)$$

Using basic trigonometric identities, we see

$$T_{n+1}(x) = \cos(n\theta) \cos(\theta) - \sin(n\theta) \sin(\theta) \quad (23)$$

$$T_{n-1}(x) = \cos(n\theta) \cos(\theta) + \sin(n\theta) \sin(\theta) \quad (24)$$

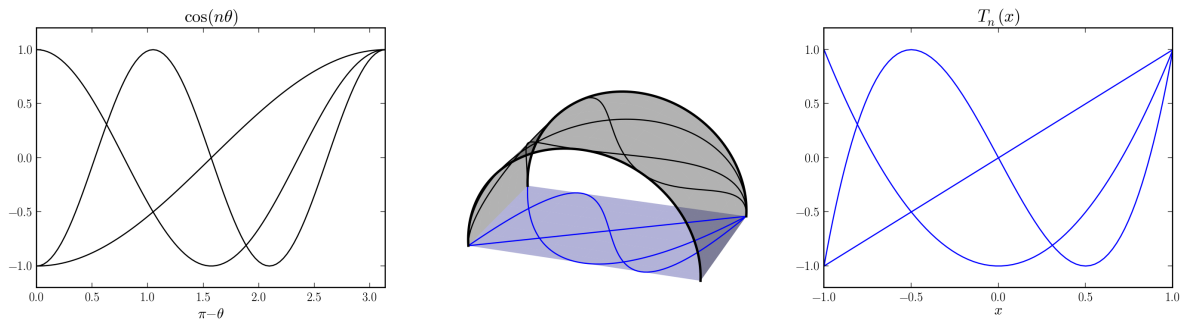


Figure 1: Chebyshev polynomials viewed as projections of cosines for  $n = 1, 2, 3$ .

$$\Rightarrow T_{n+1}(x) + T_{n-1}(x) = 2 \cos(n\theta) \cos(\theta) \quad (25)$$

$$\Rightarrow T_{n+1}(x) = 2xT_n(x) - T_{n-1}(x) \quad (26)$$

This recurrence relation, in conjunction with our expressions for  $T_0(x)$  and  $T_1(x)$ , verifies that  $T_n(x)$  is a polynomial of degree  $n$ .

The trigonometric definition of the Chebyshev polynomials provides a way of mapping a function  $f(x)$  defined on the interval  $[-1, 1]$  to a function defined over  $\theta \in \mathbb{R}^1$ , allowing us to derive the convergence properties of Chebyshev series from those of Fourier series.

**Theorem:** Chebyshev series converge exponentially for functions without singularities in  $[-1, 1]$ , whether or not the function is periodic or has singularities elsewhere on the real line.

Any Chebyshev series

$$f(x) = \sum_{n=0}^{\infty} a_n T_n(x) \quad (27)$$

can be written as

$$f(\cos(\theta)) = \sum_{n=0}^{\infty} a_n \cos(n\theta) \quad (28)$$

which is a Fourier cosine series in  $\theta$  (i.e. a Fourier series with real coefficients and  $c_n = c_{-n}$ ). The mapped function  $f(\cos(\theta))$  is  $2\pi$ -periodic in  $\theta$  and oscillates through the values of  $f(x)$  on the interval  $[-1, 1]$ , so its Fourier series converges exponentially as long as  $f(x)$  has no singularities in this interval. The same convergence follows for the Chebyshev series by the equality of the series coefficients.

**Theorem:** Let  $\{z_j = x_j + iy_j\}$  denote the set of the singularities of a function  $f(z)$ . Let  $\mu_j$  denote the quasi-radius of the  $j$ -th singularity in elliptical coordinates, i.e. the unique ellipse with foci at  $z = \pm 1$  passing through  $z_j$  has a semi-major axis  $a = \cosh(\mu_j)$ . If  $\rho$  is the smallest such quasi-radius,

$$\rho = \min_j \mu_j \quad (29)$$

then the domain of convergence of the Chebyshev series of  $f(z)$  is the ellipse with quasi-radius  $\rho$  and the asymptotic rate of convergence is  $\mu = \rho$ . Series with a finite algebraic index of convergence have  $\rho = 0$  and only converge on the real interval  $[-1, 1]$ .

The mapping of points  $\theta = \eta + i\mu$  in the complex  $\theta$  plane to the complex  $z$  plane is given by

$$z = \cos(\theta) = \cosh \mu \cos(\eta) - i \sinh(\mu) \sin(\eta) \quad (30)$$

We see that  $(\mu, \eta)$  form elliptical coordinates in the complex  $z$  plane: surfaces of constant  $\mu$  are ellipses with quasi-radius  $\mu$  and foci at  $z = \pm 1$ , as plotted in Figure 2. Since the quasi-radius of a singularity in the complex  $z$  plane is equal to the distance of the singularity from the real line in the complex  $\theta$  plane, the smallest such distance,  $\rho$ , determines the asymptotic rate of convergence of the Fourier series of  $f(\cos(\theta))$  and therefore of the Chebyshev series of  $f(z)$ . Additionally, the Fourier series converges on the strip  $|\mu| < \rho$ , which maps to the interior of the ellipse with quasi-radius  $\rho$  in the complex  $z$  plane.

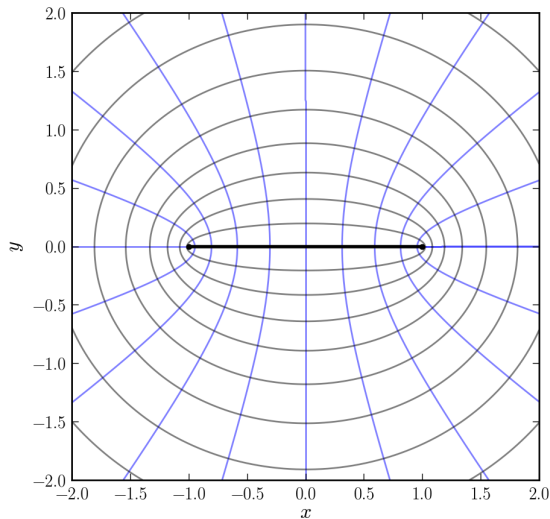


Figure 2: Surfaces of constant  $\mu$  (ellipses) and  $\eta$  (hyperbolas) in the complex  $z$  plane, under the transform  $z = \cos(\theta)$ , where  $z = x + iy$  and  $\theta = \eta + i\mu$ . The Chebyshev series of a function  $f(z)$  converges inside the smallest ellipse passing through a singularity of  $f(z)$ .

The estimates of the truncation error of a Chebyshev series using the last retained coefficient follow directly from those for Fourier series.

## 2.4 Galerkin method

Consider an ordinary differential equation

$$Hu = f \quad (31)$$

for some linear differential operator  $H$  and a known function  $f$ . The general goal of a spectral method is to approximate the true solution  $u(x)$  by a truncated series

$$u_N = \sum_{n=0}^N \alpha_n \phi_n(x) \quad (32)$$

and to find the coefficients  $\{\alpha_n\}$  that minimize the residual function

$$R(x) = Hu_N - f \quad (33)$$

**Definition:** The *Galerkin* approach to minimizing the residual function is to require that the first  $N + 1$  terms of its series expansion are zero.

The series expansion of the residual function is given by

$$R = \sum_{m=0}^{\infty} r_m \phi_m(x) \quad (34)$$

The residual coefficients can be computed via the inner product

$$r_j = (R, \phi_j) / (\phi_j, \phi_j) \quad (35)$$

where

$$(f, g) = \int_a^b \omega(x) f(x) g(x) dx \quad (36)$$

is the inner product weighted by  $\omega(x)$  on the interval  $[a, b]$  under which the basis functions are orthogonal.

Requiring  $r_i = 0$  for  $i = 0, \dots, N$  yields  $N + 1$  coupled equations for  $\alpha_0, \dots, \alpha_N$ :

$$\sum_{j=0}^N \alpha_j (\phi_i, H\phi_j) = (\phi_i, f), \quad i = 0, \dots, N \quad (37)$$

These equations can be written in matrix form as

$$\underline{\underline{H}} \cdot \underline{\alpha} = \underline{f} \quad (38)$$

where

$$H_{ij} = (\phi_i, H\phi_j) \quad (39)$$

$$f_i = (\phi_i, f) \quad (40)$$

The unknown coefficients  $\underline{\alpha}$  can be determined using a matrix solve, and the error of the approximation will be on the order of  $|r_{N+1}|$ , i.e.  $\mathcal{O}(-\mu(N+1))$  in the geometric case.

## 2.5 Pseudospectral method

While the Galerkin method is a very powerful tool, the integrals required to construct the matrix elements for Equation (39) can become prohibitively complex. If  $\{\phi_i\}$  is a polynomial basis, then the inner products required by the Galerkin method can be accurately approximated by Gaussian quadrature.

**Theorem:** Consider the set  $\{\phi_i\}$  of orthogonal polynomials on the interval  $[a, b]$  with respect to the weight  $\omega(x)$ . Then, if the set of points  $\{x_i\}$  are the  $M + 1$  zeros of  $\phi_{M+1}(x)$ , known as the  $M + 1$  *abscissas* of Gaussian quadrature, then

$$\int_a^b \omega(x) P(x) dx = \sum_{i=0}^M w_i P(x_i) = (P)_G \quad (41)$$

for all polynomials  $P(x)$  of degree less than or equal to  $2M+1$ . The quadrature weights  $\{w_i\}$  are the integrals of the cardinal functions  $\{C_i\}$  on the grid:

$$w_i = \int_a^b C_i(x) dx \quad (42)$$

$$C_i(x) = \prod_{j=0, j \neq i}^M \frac{x - x_j}{x_i - x_j} \quad (43)$$

The cardinal functions  $\{C_i\}$  on a set of  $M+1$  collocation points  $\{x_i\}$  are the unique  $M$ -th degree polynomials that satisfy  $C_i(x_j) = \delta_{ij}$ . Thus, any polynomial  $P(x)$  of degree less than or equal to  $M$  can be exactly expanded in cardinal functions as

$$P(x) = \sum_{i=0}^M P(x_i) C_i(x) \quad (44)$$

and can be exactly integrated as

$$\int_a^b P(x) dx = \sum_{i=0}^M P(x_i) \int_a^b C_i(x) dx = \sum_{i=0}^M w_i P(x_i) \quad (45)$$

Gauss's insight was that the positions of the collocation points  $\{x_i\}$  provide an additional  $M+1$  free parameters which can be adjusted to make the quadrature exact for polynomials of degree less than  $2M+1$ .

This quadrature motivates a method based on evaluating the basis functions at the collocation points.

**Definition:** The *pseudospectral* approach to minimizing the residual function is to require that it be equal to zero on the  $N+1$  abscissas of Gaussian quadrature of the given basis set.

Requiring  $R(x_i) = 0$  on the  $N+1$  abscissas  $\{x_i\}$  yields  $N+1$  coupled equations for  $\alpha_0, \dots, \alpha_N$ :

$$\sum_{j=0}^N \alpha_j H \phi_j(x_i) = f(x_i), \quad i = 0, \dots, N \quad (46)$$

or, in matrix form,

$$\underline{\underline{H}} \cdot \underline{\alpha} = \underline{f} \quad (47)$$

where

$$H_{ij} = H \phi_j(x_i) \quad (48)$$

$$f_i = f(x_i) \quad (49)$$

Multiplying each row by  $w_i \phi_n(x_i)$  and summing over  $i$  for  $n = 0, \dots, N$  yields

$$\sum_{j=0}^N \sum_{i=0}^N \alpha_j w_i \phi_n(x_i) H \phi_j(x_i) = \sum_{i=0}^N w_i \phi_n(x_i) f(x_i), \quad n = 0, \dots, N \quad (50)$$

$$\sum_{j=0}^N \alpha_j (\phi_n H \phi_j)_G = (\phi_n f)_G, \quad n = 0, \dots, N \quad (51)$$

and we see that the pseudospectral method is equivalent to the Galerkin method with the inner products evaluated via Gaussian quadrature.

Since  $H$  is a linear differential operator,  $\phi_n H\phi_j$  is a polynomial of degree less than or equal to  $2N$ , meaning it is integrated exactly by Gaussian quadrature:

$$(\phi_n H\phi_j)_G = (\phi_n, H\phi_j) \quad (52)$$

Expanding  $f(x)$  in the basis as

$$f(x) = \sum_{i=0}^N b_i \phi_i(x) + E_T(N) \quad (53)$$

we see that

$$(\phi_n f)_G = (\phi_n, f) + (\phi_n E_T(N))_G \quad (54)$$

since Gaussian quadrature honors the orthogonality and normalizations of the basis functions.

The pseudospectral method is therefore equivalent to the Galerkin method plus terms on the order of the truncation error of  $f(x)$ , which can be estimated by the last retained coefficient, i.e.  $\mathcal{O}(\exp(-\mu N))$  in the geometric case. The pseudospectral method with  $N + 1$  points is therefore roughly as accurate as the Galerkin method with  $N$  terms. Since this difference is unimportant for large  $N$ , we will use the pseudospectral method as it only requires evaluations of the basis functions and their derivatives rather than integrals as required by the Galerkin method.

### 3 Solving linear ordinary differential equations

In this section we explicitly outline the standard procedure for formulating boundary value and eigenvalue problems using the pseudospectral method with Chebyshev polynomials. These algorithms have been implemented in an open-source, object-oriented Python package and used to solve the example problems<sup>1</sup> in § 4.

#### 3.1 Selecting a grid

To quickly summarize the results of the last section: we wish to solve an ordinary differential equation of the form

$$Hu = f \quad (55)$$

where  $H$  is a linear differential operator and  $f$  is a known function. The pseudospectral method using the set of orthogonal polynomials  $\{\phi_i\}$  produces an approximate solution

$$u_N = \sum_{n=0}^N \alpha_n \phi_n(x) \quad (56)$$

by requiring that it satisfies the differential equation at the abscissas of Gaussian quadrature for the basis set.

---

<sup>1</sup>The source code for the solvers and test problems is available at <https://bitbucket.org/kburns/difftools>

Due to their convergence properties on finite intervals, we wish to use Chebyshev polynomials as our basis functions. They are orthogonal on the interval  $[-1, 1]$  under the weight

$$\omega(x) = (1 - x^2)^{-1/2} \quad (57)$$

and the corresponding abscissas for an approximation with  $N$  coefficients are the zeros of  $T_N(x)$ .

**Definition:** The *roots grid* is the set of  $N$  collocation points for Chebyshev polynomials given by the roots of  $\cos(N \arccos(x))$ ,

$$x_i = \cos\left(\frac{\pi(2i+1)}{2N}\right), \quad i = 0, \dots, N-1 \quad (58)$$

Lobatto showed that the grid composed of the extrema of  $T_N(x)$  along with the endpoints  $-1$  and  $1$  permits an integration mechanism similar to Gaussian quadrature, and thus can also be used as collocation points for the pseudospectral method with Chebyshev polynomials (Boyd, 2000).

**Definition:** The *extrema grid* is a set of  $N+1$  collocation points for Chebyshev polynomials given by the extrema of  $\cos(N \arccos(x))$  along with  $-1$  and  $1$ ,

$$x_i = \cos\left(\pi \frac{i}{N}\right), \quad i = 0, \dots, N \quad (59)$$

The extrema grid is useful because it contains the endpoints of the interval, allowing the explicit imposition of boundary conditions at those points. The roots grid is better suited if there is a singularity at an endpoint.

While both of these grids discretize the interval  $x \in [-1, 1]$ , they can be used to model any any finite interval  $\xi \in [a, b]$  via the affine transformation

$$x = \left(\xi - \frac{a+b}{2}\right) \left(\frac{2}{b-a}\right) \quad (60)$$

### 3.2 Constructing the pseudospectral matrices

The differential equation is enforced on the chosen grid by solving the  $(N+1)$  by  $(N+1)$  system

$$\underline{H} \cdot \underline{\alpha} = \underline{f} \quad (61)$$

where

$$H_{ij} = H\phi_j(x_i) \quad (62)$$

$$f_i = f(x_i) \quad (63)$$

The same framework can be used to directly solve for the values of  $u_N$  on the grid, since the same equations can be enforced on the cardinal expansion of  $u_N$ . That is, writing

$$u_N = \sum_{n=0}^N u_n C_n(x) \quad (64)$$

leads to the equivalent system

$$\underline{H} \cdot \underline{u} = \underline{f} \quad (65)$$

where

$$H_{ij} = HC_j(x_i) \quad (66)$$

The pseudospectral matrix  $\underline{H}$  is built by adding multiples of the evaluation and differentiation matrices for the proper basis set and grid, as specified by the differential operator  $H$ . Spatially varying coefficients are trivially incorporated into the construction by evaluating them at  $x_i$  in the  $i$ -th row.

**Definition:** The *evaluation matrix*  $\underline{E}$  for the basis set  $\{\phi_i\}$  on the grid  $\{x_i\}$  is given by

$$E_{ij} = \phi_j(x_i) \quad (67)$$

and is used to find the values of the approximation on the grid:

$$\underline{u} = \underline{E} \cdot \underline{\alpha} \quad (68)$$

The cardinal evaluation matrix is simply the identity, while the Chebyshev evaluation matrix is easily constructed via the trigonometric definition of the Chebyshev polynomials.

**Definition:** The  $p$ -th order *differentiation matrix*  $\underline{D}^p$  for the basis set  $\{\phi_i\}$  on the grid  $\{x_i\}$  is given by

$$D_{ij}^p = \phi_j^{(p)}(x_i) \quad (69)$$

and is used to find the  $p$ -th derivative of the approximation on the grid:

$$\underline{u}^{(p)} = \underline{D}^p \cdot \underline{\alpha} \quad (70)$$

The terms of the Chebyshev differentiation matrix can be evaluated using the Chebyshev recurrence relation, or by using the chain rule in conjunction with the trigonometric definition, as we'll outline here. With the change of variables  $x = \cos(\theta)$ , the derivative operator becomes

$$\frac{d}{dx} \rightarrow \frac{d\theta}{dx} \frac{d}{d\theta} = \frac{-1}{\sin(\theta)} \frac{d}{d\theta} \quad (71)$$

and so the derivatives of the Chebyshev polynomials can be written as

$$\frac{dT_n}{dx} = \frac{n \sin(n\theta)}{\sin(\theta)} \quad (72)$$

$$\frac{d^2 T_n}{dx^2} = -\frac{n^2 \cos(n\theta)}{\sin^2(\theta)} + \frac{n \sin(n\theta) \cos(\theta)}{\sin^3(\theta)} \quad (73)$$

for the interior points, and can be evaluated at the endpoints using L'Hopital's rule, giving

$$\frac{d^p T_n}{dx^p}(\pm 1) = (\pm 1)^{n+p} \prod_{k=0}^{p-1} \frac{n^2 - k^2}{2k + 1} \quad (74)$$

The derivatives of the cardinal functions on the roots grid are

$$\frac{dC_j}{dx}(x_i) = \begin{cases} \frac{x_j}{2(1-x_j^2)} & i = j \\ (-1)^{i+j} \frac{\sqrt{(1-x_j^2)/(1-x_i^2)}}{x_i - x_j} & i \neq j \end{cases} \quad (75)$$

and the derivatives on the extrema grid are

$$\frac{dC_j}{dx}(x_i) = \begin{cases} (1+2N^2)/6 & i = j = 0 \\ -(1+2N^2)/6 & i = j = N \\ -\frac{x_j}{2(1-x_j^2)} & i = j, 0 < j < N \\ (-1)^{i+j} \frac{c_i}{c_j(x_i - x_j)} & i \neq j \end{cases} \quad (76)$$

$$c_i = \begin{cases} 2 & i = 0, N \\ 1 & i = 1, \dots, N-1 \end{cases} \quad (77)$$

as given in the appendix of [Boyd](#). Higher derivatives for the cardinal bases can be constructed by repeatedly dotting  $D^1$  with itself, since the values on the grid are the same as the cardinal series coefficients.

For problems defined on the interval  $\xi \in [a, b]$ , the affine transformation to the Chebyshev domain includes a scaling factor of  $2/(b-a)$ , so the derivative matrices must be scaled from those on the regular domain as

$$\underline{\underline{D}}_{\xi}^p = \left( \frac{2}{a-b} \right)^p \underline{\underline{D}}^p \quad (78)$$

### 3.3 Generalized eigenvalue equations

In addition to the boundary value problems outlined so far, the pseudospectral framework can also be used to solve generalized eigenvalue problems of the form

$$Hu = \lambda Gu \quad (79)$$

where  $H$  and  $G$  are linear differential operators and  $\lambda$  is an unknown eigenvalue. Such systems can be written in matrix form as

$$\underline{\underline{H}} \cdot \underline{\alpha} = \lambda \underline{\underline{G}} \cdot \underline{\alpha} \quad (80)$$

$$H_{ij} = H\phi_j(x_i) \quad (81)$$

$$G_{ij} = G\phi_j(x_i) \quad (82)$$

This system can then be solved for the unknown coefficients  $\underline{\alpha}$  using routines commonly found in linear algebra libraries.

### 3.4 Implementing boundary conditions

There are two main strategies for implementing boundary conditions: boundary bordering and basis recombination.

**Definition:** The *boundary bordering* method consists of replacing the collocation condition (i.e. the requirement that the differential equation is satisfied) near the boundaries with enforcement of the boundary conditions.

The boundary bordering method simply entails replacing the  $i$ -th row of the pseudospectral system with the boundary condition at  $x_i$ . For multiple conditions at the same point, the collocation requirement for the nearest neighboring points are replaced with the additional conditions.

This method is a straightforward way of implementing many forms of boundary conditions. For instance, implementing the inhomogeneous Dirichlet condition at the right boundary

$$u(x_0) = \alpha \quad (83)$$

is achieved by setting

$$H_{0j} = \phi_j(x_0), \quad j = 0, \dots, N \quad (84)$$

$$f_0 = \alpha \quad (85)$$

To additionally implement the inhomogeneous Neumann condition

$$\frac{du}{dx}(x_0) = \beta \quad (86)$$

we replace the collocation condition at  $x_1$  by setting

$$H_{1j} = \frac{d\phi_j}{dx}(x_0), \quad j = 0, \dots, N \quad (87)$$

$$f_1 = \beta \quad (88)$$

If the set of basis functions already satisfies the desired boundary conditions, then no adjustments would be necessary.

**Definition:** The *basis recombination* method consists of using linear combinations of the  $N + 1$  basis functions to form a new set of  $N + 1 - B$  basis functions that individually satisfy  $B$  boundary conditions.

The pseudospectral method on  $N + 1 - B$  of the collocation points, using the recombined basis functions, will produce “recombined” coefficients which can be used to construct the spectral coefficients of an approximate solution satisfying the boundary conditions.

For instance, for homogeneous Dirichlet conditions at both endpoints, we could use the basis

$$\phi_n(x) = \begin{cases} T_n(x) - 1 & i = 2, 4, \dots \\ T_n(x) - x & i = 3, 5, \dots \end{cases} \quad (89)$$

since these functions individually satisfy  $\phi_i(-1) = \phi_i(1) = 0$ . Solving the resulting system on the points  $\{x_i : i = 1, \dots, N - 1\}$  yields the recombined coefficients  $\{\alpha_i : i = 2, \dots, N\}$ . The Chebyshev coefficients of the solution can then be reconstructed from the definition of the this “double-Dirichlet” basis as

$$a_n = \begin{cases} -\sum_{i=1}^{2i \leq N} \alpha_{2i} & n = 0 \\ -\sum_{i=1}^{(2i+1) \leq N} \alpha_{2i+1} & n = 1 \\ \alpha_n & n = 2, \dots, N \end{cases} \quad (90)$$

Examining the expression for the derivatives of the Chebyshev polynomials at the endpoints, one can construct the following basis for homogeneous Neumann conditions at both endpoints:

$$\phi_n(x) = \begin{cases} 1 & i = 0 \\ T_n(x) - \left(\frac{i}{i+2}\right)^2 T_{n+2}(x) & i = 1, \dots, N-2 \end{cases} \quad (91)$$

Basis recombination produces slightly smaller matrices than boundary bordering, but the latter is easier to implement for more complicated boundary conditions. Basis recombination is preferable in eigenvalue problems unless the boundary conditions involve the eigenvalues, since numerical eigenvalue solvers are best suited to systems with the eigenvalue in every row (Boyd, 2000).

### 3.5 Solving systems of equations

The pseudospectral framework can also be easily extended to systems of equations. A system of  $M$  equations for  $M$  unknown functions is formed using the block matrices

$$\underline{\underline{K}} \cdot \underline{A} = \underline{F} \quad (92)$$

$\underline{\underline{K}}$  is a matrix of size  $(M(N+1)) \times (M(N+1))$ , made up of submatrices  $K^{k,l}$  of size  $(N+1) \times (N+1)$  that represent the differential operator acting on the  $l$ -th variable in the  $k$ -th equation.  $\underline{A}$  is a vector of length  $M(N+1)$ , made up of length  $N+1$  subvectors  $A^l$  that are the coefficients of the  $l$ -th variable. For boundary value problems,  $\underline{F}$  is also a vector of length  $M(N+1)$  whose  $l$ -th subvector is the right-hand-sides of the  $l$ -th equation. This formulation can also be extended to eigenvalue problems, where the right-hand side is another block matrix representing all the terms involving the eigenvalue.

For example, consider the following system for the two unknown functions  $u$  and  $v$ , whose coefficients are given by  $\{\alpha_i\}$  and  $\{\beta_i\}$ , respectively:

$$H_1 u + H_2 v = f_1 \quad (93)$$

$$H_3 u + H_4 v = f_2 \quad (94)$$

The system matrices and vectors are then given by

$$\underline{\underline{K}} = \begin{pmatrix} \underline{H1} & \underline{H2} \\ \underline{H3} & \underline{H4} \end{pmatrix} \quad (95)$$

$$\underline{A} = \begin{pmatrix} \underline{\alpha} \\ \underline{\beta} \end{pmatrix} \quad (96)$$

$$\underline{F} = \begin{pmatrix} \underline{f_1} \\ \underline{f_2} \end{pmatrix} \quad (97)$$

## 4 ODE Examples

The pseudospectral method of solving linear ordinary differential equations as described in § 3 is applied to several problems. In the first example, finding the eigenmodes of a plucked string, analytic solutions exist and allow us to examine the exact errors of our pseudospectral approach. In the second and third examples, we find the normal modes of two astrophysical flows by following published results.

### 4.1 Plucked string

To verify the implementation of the algorithms described above, we examined the eigenvalue equation for disturbances to a string fixed at the ends of the interval  $[0, 1]$ :

$$\frac{d^2 y}{dx^2} + \lambda y = 0 \quad (98)$$

$$y(0) = y(1) = 0 \quad (99)$$

The corresponding pseudospectral system was set up using the double-Dirichlet recombined basis on the extrema grid. The system takes the form described in § 3.3:

$$\underline{\underline{H}} \cdot \underline{\alpha} = \lambda \underline{\underline{G}} \cdot \underline{\alpha} \quad (100)$$

with

$$\underline{\underline{H}} = \underline{\underline{D}}^2 \quad (101)$$

$$\underline{\underline{G}} = -\underline{\underline{E}} \quad (102)$$

The exact eigenmodes of the equation are

$$y_j = \sin(\pi j x), \quad j = 1, 2, \dots \quad (103)$$

with corresponding eigenvalues

$$\lambda_j = \pi^2 j^2 \quad (104)$$

The pseudospectral system was solved with 32 and 64 points. Figure 3 shows the absolute errors in the numerically computed eigenvalues. We note that for both resolutions, roughly the first  $N/2$  eigenvalues have an “acceptable” error of less than 0.01 and roughly the first  $N/3$  are accurate to within roundoff error. Higher eigenvalues are not accurately computed because the corresponding eigenfunctions are not well resolved by the modes included in the calculation. Figure 4 compares the 5th and 20th eigenmodes, as computed with 32 collocation points, to the corresponding exact solutions. The 20th mode is not sufficiently resolved by the grid, yielding a *numerically spurious* eigenvalue whose accuracy can only be improved by increasing the resolution.

These results closely match those in § 7.3 of Boyd, where the same problem is examined using 16 and 32-point calculations.

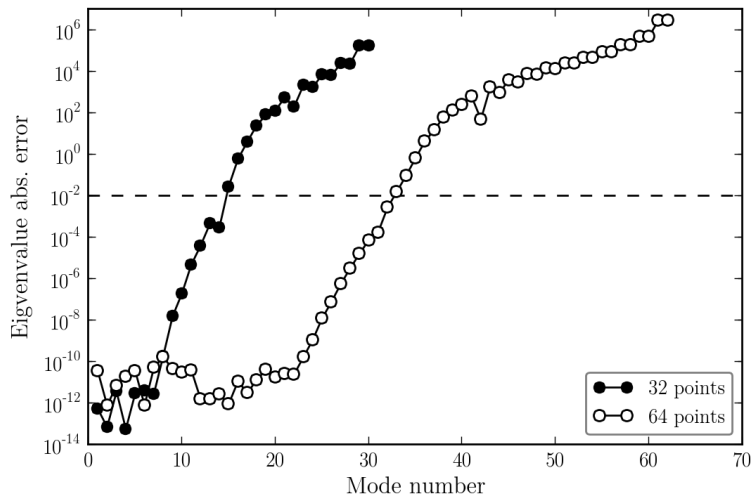


Figure 3: Errors in the eigenvalues of a plucked string as computed with 32 and 64-point pseudospectral discretizations.

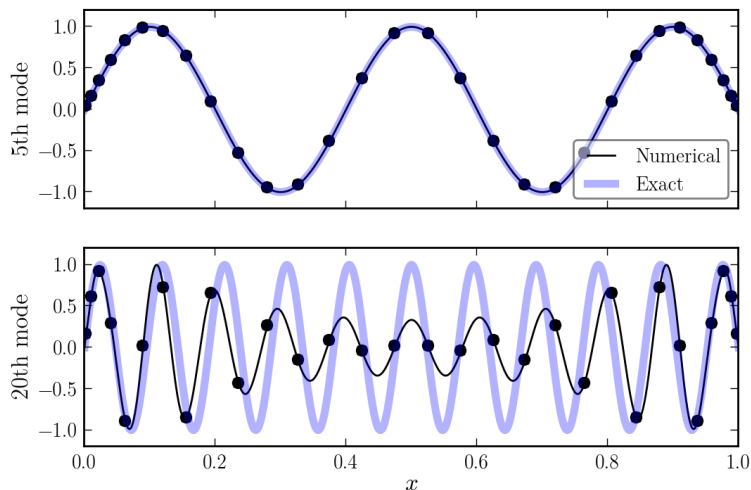


Figure 4: Exact and computed eigenmodes of a plucked string as found using a 32-point pseudospectral discretization.

## 4.2 Stratified magnetorotational instability

The magnetorotational instability (MRI) is a linear instability that occurs in differentially rotating discs threaded by a vertical magnetic field. It was discovered in 1991 by Balbus and Hawley, and leads to magnetohydrodynamic (MHD) turbulence capable of transporting significant amounts of angular momentum through the disc. Simulations of the MRI in unstratified shearing boxes are dominated by planar channel flows, and [Latter et al. \(2010\)](#) show that such modes also exist in stratified disc models, and examine their vertical structure using pseudospectral techniques.

They begin with the ideal MHD equations in the shearing sheet approximation and a corresponding equilibrium state with a vertical background magnetic field. They then introduce non-linear perturba-

tions to the background velocity and magnetic field given by

$$\underline{u}_{ch} = bu_0 F \exp(st) [\underline{e}_x \cos(\theta) + \underline{e}_y \sin(\theta)] \quad (105)$$

$$\underline{B}_{ch} = bB_0 G \exp(st) [\underline{e}_x \sin(\theta) - \underline{e}_y \cos(\theta)] \quad (106)$$

where  $b$  is the ratio between the initial perturbations and the background velocity and magnetic field amplitudes,  $u_0$  and  $B_0$ ,  $s$  is the growth rate,  $\theta$  describes the flow's orientation, and  $F$  and  $G$  are dimensionless envelope functions that depend on the height  $z$  out of the disc. Linearizing the governing equations leads to a system for the envelop functions

$$F = -\frac{1}{Kh} \frac{dG}{dz} \quad (107)$$

$$G = \frac{1}{K} \frac{dF}{dz} \quad (108)$$

where  $h$  is a dimensionless function describing the vertical density profile of the disc,  $K$  is the unknown vertical wavenumber, and  $G \rightarrow 0$  at the boundaries of the disc. For a polytropic disc with an adiabatic index of 5/3, the density profile is  $h = (1 - z^2/H^2)^{3/2}$ , where  $H$  is the height of the surface of the disc.

We solved for the eigenmodes in this case by writing the system as a single second order equation

$$\frac{d^2 F}{dz^2} + K^2 h F = 0 \quad (109)$$

$$\frac{dF}{dz}(\pm 1) = 0 \quad (110)$$

and applying the pseudospectral method with the double-Neumann recombined basis on the extrema grid with 128 points. Since we do not have analytical answers for comparison, the system was also solved using 160 grid points. We then calculated the eigenvalue drift

$$\delta_j = |\lambda_j(N_1) - \lambda_j(N_2)|/\sigma_j \quad (111)$$

where the normalization is the difference between adjacent eigenvalues

$$\sigma_j = \begin{cases} |\lambda_1(N_1) - \lambda_2(N_1)| & j = 1 \\ (|\lambda_j(N_1) - \lambda_{j-1}(N_1)| + |\lambda_{j+1}(N_1) - \lambda_j(N_1)|)/2 & j > 1 \end{cases} \quad (112)$$

The eigenvalue drift provides a measurement of how much increasing the resolution affects the eigenvalues relative to the spacing between them, and is plotted in Figure 5. Since the eigenvalues of well-resolved eigenmodes should be insensitive to increases in the resolution, we conclude that the first 40 eigenmodes (those with very small drifts) are properly resolved.

The first four and 10th eigenfunctions of  $F$  (solved for directly) and  $G$  (from Equation (108)) as computed with 128 grid points are shown in Figure 6. The eigenfunctions and corresponding eigenvalues (wavenumbers) match those computed by [Latter et al.](#) via a shooting method. They go on to confirm the growth of such modes using 1D MHD simulations, and study the parasitic instabilities that eventually destroy the growing channel modes and result in turbulence.

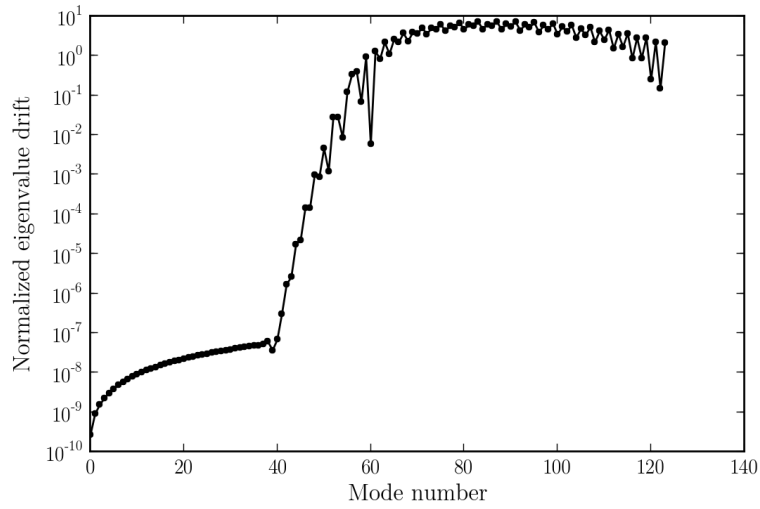


Figure 5: Eigenvalue drifts between 128 and 160-point pseudospectral approximations to the eigenmodes of the MRI in a stratified disc.

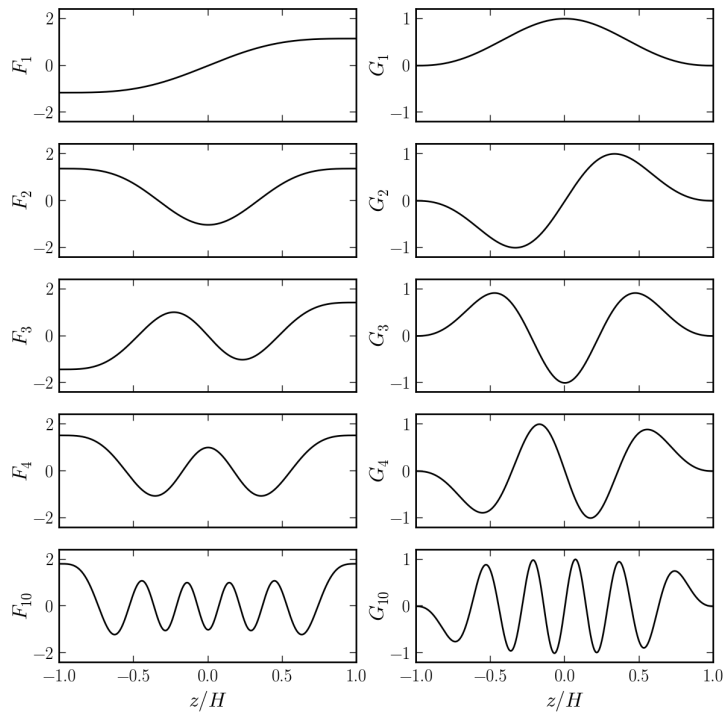


Figure 6: Eigenmodes of the MRI in a stratified disc as computed with a 128-point pseudospectral approximation.  $F$  and  $G$  are envelope functions describing the vertical structure of perturbations to the background velocity and magnetic fields, respectively.

### 4.3 Plane-parallel heat-flux buoyancy instability

X-ray emission from the intracluster medium (ICM) indicates that galaxy cluster cores should be cooling on timescales substantially shorter than the Hubble time. Corresponding cooling flows into the cores are not observed, however, so some other heating mechanism must be maintaining the temperature in the core. Since the ICM is a weakly collisional plasma (the ion gyroradius is much smaller than the collisional mean free path of particles), heat conduction occurs mainly along magnetic field lines. Along with the radial temperature gradient, this leads to a heat-flux driven buoyancy instability (HBI) which may prevent heat conduction into the core via field-line insulation.

The weakly collisional nature of the ICM also leads to strong pressure anisotropy with respect to the local magnetic field. [Latter and Kunz \(2012\)](#) study how this modifies HBI modes in a plane-parallel atmosphere model that aims to capture the radial structure of the ICM. They begin with an equilibrium state calculated from the Braginskii-MHD equations, and introduce two-dimensional perturbations

$$\rho_1, T_1, \underline{v}_1 = (u_1, 0, w_1), \underline{B}_1 = \left(-\frac{dA_1}{dz}, 0, \frac{dA_1}{dz}\right) \propto f(z) \exp(\sigma t + ikx) \quad (113)$$

to the density, temperature, velocity field, and magnetic field, respectively, where  $\sigma$  is a complex growth rate and  $k$  is a real wavenumber. The resulting system, after linearization and non-dimensionalization, is

$$\sigma \frac{\rho_1}{\rho_0} = -iku_1 - \left(\frac{d \ln(\rho_0)}{dz} + \frac{d}{dz}\right) w_1 \quad (114)$$

$$\sigma u_1 = -ikT_0 \left(\frac{\rho_1}{\rho_0} + \frac{T_1}{T_0}\right) + \frac{2}{\beta(0)\rho_0} \left(k^2 - \frac{d^2}{dz^2}\right) A_1 - \frac{ik}{\mathcal{R}e} \frac{T_0^{5/2}}{\rho_0} \left(\frac{2}{3} \frac{dw_1}{dz} - \frac{1}{3} iku_1\right) \quad (115)$$

$$\sigma w_1 = -T_0 \frac{d}{dz} \frac{\rho_1}{\rho_0} - T_0 \left(\frac{d \ln p_0}{dz} + \frac{d}{dz}\right) \frac{T_1}{T_0} + \frac{2}{\mathcal{R}e} \frac{T_0^{5/2}}{\rho_0} \left(\frac{5}{2} \frac{d \ln T_0}{dz} + \frac{d}{dz}\right) \left(\frac{2}{3} \frac{dw_1}{dz} - \frac{1}{3} iku_1\right) \quad (116)$$

$$\sigma \frac{3}{2} \frac{T_1}{T_0} = -iku_1 - \left(\frac{3}{2} \frac{d \ln T_0}{dz} + \frac{d}{dz}\right) w_1 + \frac{1}{p_0 \mathcal{P}e} \left[\frac{d^2}{dz^2} \left(T_0^{7/2} \frac{T_1}{T_0}\right) + q_b ik \frac{dA_1}{dz}\right] \quad (117)$$

$$\sigma A_1 = -u_1 \quad (118)$$

where

$$T_0 = (1 + \zeta z)^{2/7} \quad (119)$$

$$P_0 = \exp\left\{-\frac{7}{5} \frac{G}{\zeta} [(1 + \zeta z)^{5/7} - 1]\right\} \quad (120)$$

$$\rho_0 = \frac{p_0}{T_0} \quad (121)$$

are the background temperature, pressure, and density profiles, with  $\zeta = [(T_0(1)/T_0(0))^{7/2} - 1]$  and  $q_b = -(2/7)\zeta$  measuring the heat flux through the atmosphere. The Reynolds and Peclet numbers control the strength of viscous and thermal transport, and can be written as  $\mathcal{R}e = 2.08G/K$  and  $\mathcal{P}e = 0.042G/K$ , where  $G$  is the number of thermal-pressure scale heights in our model and  $K$  is ratio of this scale height to the particle mean free path. Finally,  $\beta$  is the plasma beta. Our calculations use

$\beta(0) = 10^5$ ,  $G = 2$ ,  $K = 1/1500$ , and  $T_0(1)/T_0(0) = 2.5$ .

Not allowing penetration at the boundaries results in homogeneous Dirichlet conditions for  $w_1$ . Constraining the magnetic field to be vertical at the boundaries results in homogeneous Neumann conditions on  $A_1$  and  $u_1$ . Enforcing constant temperatures at the boundaries,  $T(0) = T_0(0)$  and  $T(1) = T_0(1)$ , results in homogeneous Dirichlet conditions for  $T_1$ . The corresponding recombined bases were used, and this system of five equations for the eigenvalues  $\sigma$  was solved as described in § 3.5.

In Figure 7 we plot the real part of the 10 largest eigenvalues for a range of horizontal wavenumbers. The calculation was repeated while increasing the resolution until the depicted growth rates were stable. The results for 128 grid points are shown. Coalescence into conjugate pairs and bifurcation into purely real modes is seen.

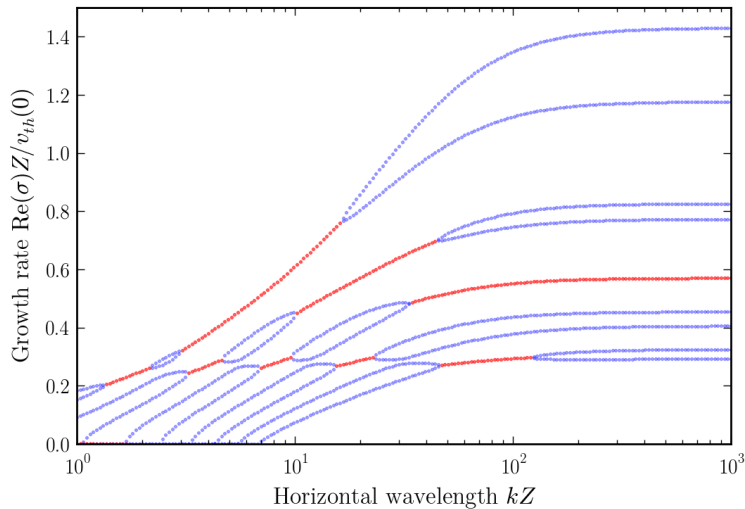


Figure 7: Growth rates of HBI modes in a plane parallel atmosphere, as computed with 128-point pseudospectral approximations. Blue dots indicate purely real growth rates, while red dots indicate conjugate pairs.

Figure 8 shows the eigenfunctions of the fourth fastest growing mode with a horizontal wavenumber  $k = 250$ . The plots indicate that the perturbations are largely confined to small heights, due to steeper temperature gradients and lower viscous damping there. These results match those shown in Figures 2 and 3 of [Latter and Kunz \(2012\)](#). They conclude that the HBI and associated field-line insulation may be limited to just the innermost regions of cluster cores, allowing heat conduction to balance radiative losses in most of the surrounding volume.

## 5 Solving partial differential equations

This section outlines the use of spectral methods for solving initial value problems with one spatial and one temporal dimension. The approach is to construct the time derivative by spectrally evaluating any spatial derivatives in the problem, and then using an explicit ODE integrator to march the solution forward in time<sup>2</sup>. These steps can take place either in the modal space (“k-space”) using the Chebyshev coefficients, or equivalently in the nodal space (“x-space”) using the values on the grid. The choice

<sup>2</sup>Implicit methods are also commonly used. They are more stable than explicit methods for longer timesteps, but require solving a dense system at every iteration

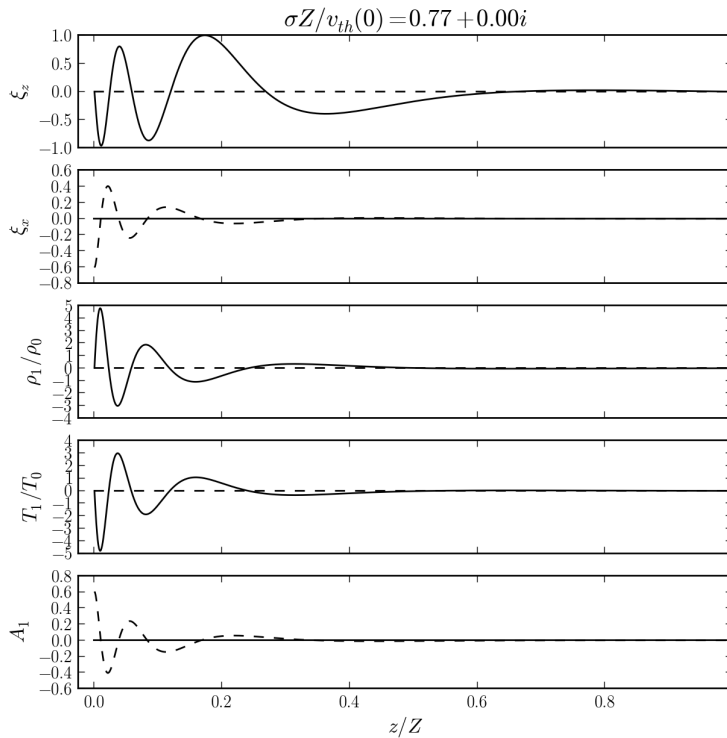


Figure 8: The fourth fastest growing eigenmode of the HBI in a plane parallel atmosphere, as computed with 250-point pseudospectral approximations. The solid lines represent the real parts of the eigenmodes, and the solid lines represent the imaginary parts.

of differentiation and integration spaces may depend on the form of the differential equation and the problem size.

## 5.1 Constructing the time derivative

We consider an initial value problem of the form:

$$\frac{du}{dt} = Hu + f(x) \quad (122)$$

where  $H$  is a differential operator (not necessarily linear) and  $f$  is a known function. Constructing any necessary spatial derivatives in  $x$ -space simply involves using the cardinal differentiation matrices as described in § 3.2, i.e.

$$\underline{u}^{(p)} = \underline{\underline{D}}^p \cdot \underline{u} \quad (123)$$

Constructing derivatives in  $k$ -space can be achieved via a recurrence relation (Boyd, 2000). Writing

$$\frac{du}{dx} = \sum_{n=0}^N b_n T_n \quad (124)$$

we can compute the coefficients of the derivative from those of the function itself, in descending order,

as

$$b_N = 0 \quad (125)$$

$$b_{N-1} = 2Na_N \quad (126)$$

$$b_n = 2(n+1)a_{n+1} + b_{n+2}, \quad n = N-2, \dots, 1 \quad (127)$$

$$b_0 = a_1 + b_2/2 \quad (128)$$

Higher derivatives are computed by repeated application of the recursion relation.

For  $N$  collocation points, the k-space recursion derivative has an  $\mathcal{O}(N)$  cost while the dense matrix multiplication in the x-space derivative is a much more expensive  $\mathcal{O}(N^2)$  operation. However, any non-linear terms or terms involving spatially varying coefficients should be computed in x-space with point-by-point multiplication ( $\mathcal{O}(N)$ ) rather than in k-space, where a Cauchy product is required ( $\mathcal{O}(N^2)$ ). The ideal strategy, at least for large  $N$ , would be to compute derivatives in k-space and non-linear products in x-space. However, transitioning from the series coefficients to the values on the grid via the evaluation matrix is also an  $\mathcal{O}(N^2)$  operation.

The solution lies in the trigonometric definition of the Chebyshev polynomials. Since the Chebyshev collocation points are evenly spaced in  $\theta = \arccos(x)$ , the series coefficients of the cosine series of  $u(\cos(\theta))$  can be computed from the grid values, and vice versa, via the discrete cosine transform<sup>3</sup>. On the extrema grid, for instance, we have

$$u_j = \sum_{n=0}^N a_n \cos\left(\frac{\pi j n}{N}\right), \quad j = 0, \dots, N \quad (129)$$

$$a_n = \frac{2}{c_n N} \sum_{j=0}^N \frac{u_j}{c_j} \cos\left(\frac{\pi j n}{N}\right), \quad n = 0, \dots, N \quad (130)$$

where  $c_j = 1 + \delta_{j0} + \delta_{jN}$ . The transform itself can be computed in  $\mathcal{O}(N \ln(N))$  time using a modified version of the Fast Fourier Transform (FFT).

## 5.2 Explicit time marching

Once the time derivatives have been constructed, the problem has been transformed into a system of  $N$  ordinary differential equations in time, which can be integrated using a variety of methods, including multistep and Runge-Kutta algorithms. We generally make use of *embedded* Runge-Kutta algorithms, which automatically adjust the timestep to try to maintain a desired accuracy.

A  $q$ -th order Runge-Kutta algorithm integrates a system by using a linear combination of the derivative as evaluated at  $q$  intermediate stages, and can be thought of as higher-order generalizations of the simple forward Euler algorithm

$$u(t + dt) = u(t) + h \frac{du}{dt}(t) \quad (131)$$

with timestep  $h$ .

A  $q$ -th order Runge-Kutta algorithm will have an error per iteration of  $\epsilon \sim \mathcal{O}(h^{q+1})$ . An embedded Runge-Kutta scheme generally uses  $q+1$  stages to construct one  $q$ -th order and one  $(q+1)$ -th order

<sup>3</sup>The type-1 DCT is used for the extrema grid, and the type-2 DCT is used for the roots grid.

step, and takes the difference between them as  $\epsilon_q$ , the error of the  $q$ -th order step. Assuming the error behaves like  $Ch^{q+1}$  for some constant  $C$ , we find

$$C \approx \frac{\epsilon_q}{h^{q+1}} \quad (132)$$

This approximation can then be used to determine a new timestep,  $h_e$ , that would produce an error equal to a user-specified tolerance per unit timestep,  $\tau$ :

$$Ch_e^{q+1} = \tau h_e \quad (133)$$

$$\implies h_e = \left(\frac{\tau}{C}\right)^{1/q} \quad (134)$$

If the error  $\epsilon_q$  was less than  $\tau h$ , then the solution is updated using the  $q$ -th order step, and the next step is taken using the new timestep  $h_e$ . Otherwise, the step is rejected and recomputed with the timestep  $h_e$ .

### 5.3 Modified grids

For equations with higher order spatial derivatives, the stability of explicit methods is severely limited by the spurious eigenvalues of the Chebyshev differentiation matrices. The size of the largest eigenvalues of  $\underline{D}$  scale as  $\mathcal{O}(N^2)$ , meaning that the limiting timestep for stability scales as  $\mathcal{O}(N^{-2p})$  for an equation with derivatives up to order  $p$ .

The scaling of the spurious eigenvalues is thought to be related to the bunching of the Chebyshev collocation points near the endpoints (the smallest spacing on the Chebyshev grid goes as  $\mathcal{O}(N^{-2})$ ). [Kosloff and Tal-Ezer \(1993\)](#) propose a remapping of the collocation points via

$$\xi_i = \frac{\arcsin(\alpha x_i)}{\arcsin \alpha} \quad (135)$$

This mapping produces an evenly spaced grid when  $\alpha = 1$ , and reduces to the original Chebyshev grid when  $\alpha = 0$ . They also prove that if

$$\alpha = 1 - \frac{C}{N^2} + \mathcal{O}(N^{-3}) \quad (136)$$

for some constant  $C$ , then the minimum spacing on the grid scales like  $\mathcal{O}(N^{-1})$  as  $N \rightarrow \infty$ . This is postulated to reduce the largest eigenvalue of the differentiation matrix to  $\mathcal{O}(N)$ , and hence improve the limiting timestep for a  $p$ -th order equation to  $\mathcal{O}(N^{-p})$ . We verify these scalings in [Figure 9](#), where we plot the magnitude of the largest eigenvalues of  $\underline{D}$  for the extrema grid and for the remapped grid using  $\alpha = \cos(1/N)$ .

There is, however, a major drawback to this grid: the mapping in [Equation \(135\)](#) has branch points at  $\pm\alpha^{-1}$ . Thus, sending  $\alpha \rightarrow 1$  improves the time-marching stability as the points spread more uniformly across the domain, but simultaneously decreases the asymptotic rate of geometric convergence as the poles of the mapping approach the interval  $[-1, 1]$ . We verified this by expanding the entire function

$$u(x) = \cos(\pi x) \quad (137)$$

using 64 points over the original Chebyshev extrema grid, the remapped grid with  $\alpha = \cos(1/2)$ , and the remapped grid with  $\alpha = \cos(1/N)$ . The magnitudes of the (even) coefficients are plotted in [Figure 10](#). As

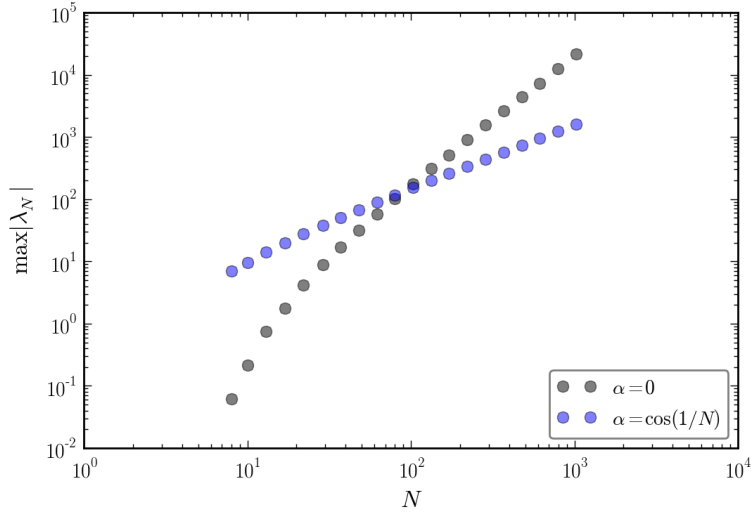


Figure 9: The magnitude of the largest eigenvalues of the differentiation matrices for the Chebyshev extrema grid and the remapped Kosloff grid.

expected, the series converges supergeometrically on the original grid. However, it converges much slower on the remapped grids, at rates approaching the expected asymptotic values satisfying  $\cosh(\mu) = 1/\alpha$ .

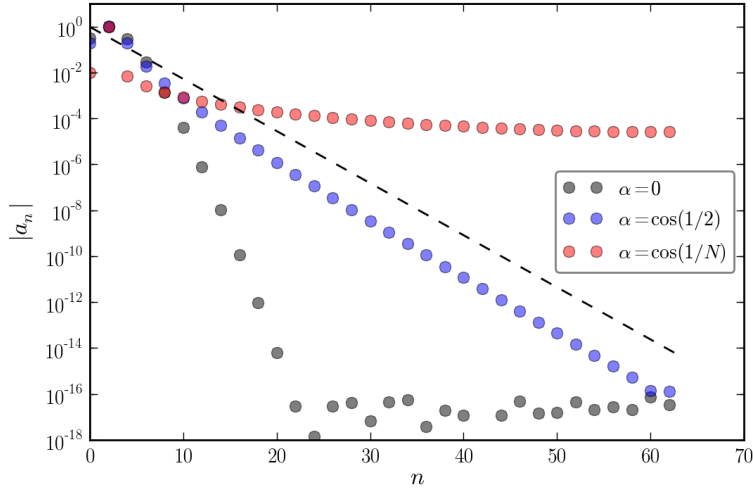


Figure 10: The convergence of the expansion of the entire function  $u(x) = \cos(\pi x)$  on the Chebyshev extrema grid and the remapped Kosloff grid. Only the even coefficients are shown, since the odd coefficients are all zero by symmetry. The dashed curve indicates the expected asymptotic rate of geometric convergence for the  $\alpha = \cos(1/2)$  case.

Boyd suggests the use of a constant remapping parameter, such as  $\alpha = \cos(1/2)$  as a compromise between spectral accuracy and stability for larger timesteps. The locations of the eigenvalues of  $\underline{D}$  in the complex plane, for the original extrema grid and the remapped grid with this value of  $\alpha$ , are shown in Figure 11, demonstrating that a substantial reduction in the eigenvalue magnitudes can be achieved while still retaining acceptable geometric convergence as shown in Figure 10.

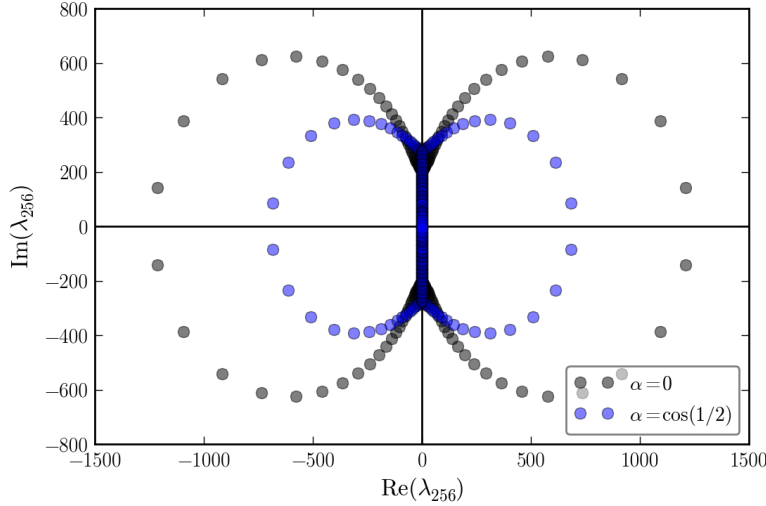


Figure 11: The eigenvalues of 256-point differentiation on the Chebyshev extrema grid and the remapped Kosloff grid.

#### 5.4 Implementing boundary conditions

When implicitly solving for the  $N$  series coefficients, it is possible to produce a solution that simultaneously satisfies the collocation condition at  $N - B$  collocation points as well as  $B$  boundary conditions. Using an explicit method requires a different strategy. Since the explicitly computed time derivative will not generally satisfy the desired boundary conditions, after every iteration<sup>4</sup> the solution must be modified to satisfy the boundary conditions.

One method to satisfy the Dirichlet condition,

$$u(x_i) = \alpha \quad (138)$$

is to just explicitly set  $u_i = \alpha$ . If  $u_i = \chi$  before updating the new solution, then this is equivalent to adding  $(\alpha - \chi)C_i$  to solution. Using Equation (130), we can perform such an update in k-space as

$$a_n \rightarrow a_n + \frac{2(\alpha - \chi)}{c_i c_n N} \cos\left(\frac{\pi i n}{N}\right) \quad (139)$$

possibly avoiding an FFT just to enforce the boundary condition. While this *global coefficient adjustment* only changes the value of the solution at  $x_i$ , it introduces a small error into the residuals at all of the grid points, since the derivative of  $C_i$  on the grid is nonzero (see Figure 12).

Satisfying the Neumann condition

$$u(x_i) = \beta \quad (140)$$

is more complicated. Common strategies include modifying the value at the boundary according to a low-order finite difference approximation<sup>5</sup> or by modifying the highest coefficient  $a_N$  to meet the condition. Here, the last coefficient is modified since  $T_N$  has the largest derivative at the boundaries, meaning  $a_N$  would have to be adjusted by a smaller amount than would any other coefficient.

<sup>4</sup>and at every stage of a Runge-Kutta step

<sup>5</sup>For instance, setting  $u_i = u_{i\pm 1} - (x_{i\pm 1} - x_i)\beta$

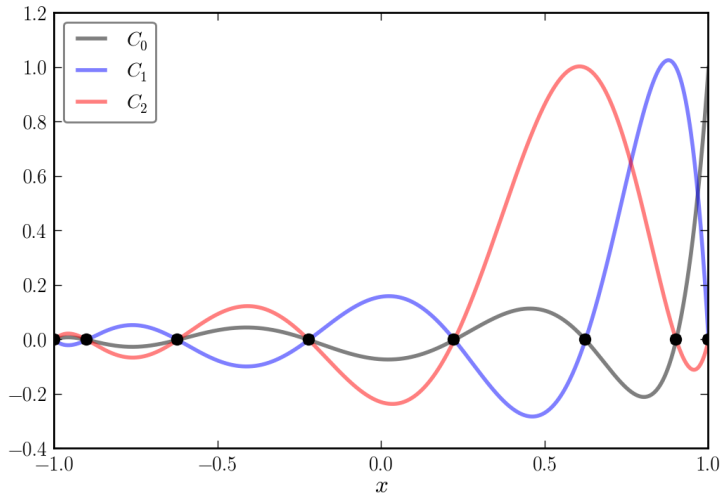


Figure 12: The first three cardinal polynomials on the 8-point extrema grid.

Wang et al. (1993) point out that this method modifies the value at every grid point by the same magnitude, since the grid points are located at the extrema of  $T_N$ . Instead, they propose modifying the value at  $x_i$  so that the interpolating polynomial satisfies the condition, as in the Dirichlet case. If  $\frac{du}{dx}(x_i) = \gamma$  before adjustment, the condition is enforced by adding  $\delta C_i$  to the solution, where

$$\delta = (\beta - \gamma) \left( \frac{dC_i}{dx}(x_i) \right)^{-1} \quad (141)$$

Again, this method perturbs the residuals at the grid points by modifying the derivative there, but this effect decays as away from the boundary instead of remaining uniform across the grid. It can easily be implemented in both x-space and k-space just as in the Dirichlet case.

However, if the equation requires a Dirichlet and a Neumann condition to be imposed at the same grid point, this method fails as it would require two generally incompatible values at the endpoint. After enforcing the Dirichlet condition by adding a multiple of  $C_i$ , however, we can still affect the derivative at the endpoint without changing the value there by adding another cardinal polynomial. The cardinal polynomial corresponding to the first interior point,  $C_j$ , where  $(i, j) = (0, 1)$  at the right boundary and  $(i, j) = (N, N - 1)$  at the left, is the natural choice: it has a larger derivative at  $x_i$  than the other available cardinal polynomials, meaning the grid adjustment required here is smaller than elsewhere, and we presume that the boundary conditions should primarily dictate behavior more strongly near the boundary than away from it. Therefore, after enforcing the Dirichlet condition at  $x_i$ , we propose to enforce the Neumann condition there by adding  $\delta C_j$  to the solution, where

$$\delta = (\beta - \gamma) \left( \frac{dC_j}{dx}(x_i) \right)^{-1} \quad (142)$$

Finally, consider a fourth order equation with double Dirichlet and Neumann conditions. The Dirichlet conditions are imposed by adding multiples of  $C_0$  and  $C_N$ . However, sequentially imposing the Neumann conditions using  $C_1$  and  $C_{N-1}$  as described above fails because the derivatives of  $C_1$  and  $C_{N-1}$  are non-zero at  $x_N$  and  $x_0$ , respectively. Simultaneously enforcing the conditions requires solving the system

$$\epsilon_0 = \delta_1 \frac{dC_1}{dx}(x_0) + \delta_{N-1} \frac{dC_{N-1}}{dx}(x_0) \quad (143)$$

$$\epsilon_N = \delta_1 \frac{dC_1}{dx}(x_N) + \delta_{N-1} \frac{dC_{N-1}}{dx}(x_N) \quad (144)$$

for the necessary grid value adjustments  $\delta_1$  and  $\delta_{N-1}$ , where  $\epsilon_0$  and  $\epsilon_N$  are the derivative adjustments required to satisfy the Neumann conditions at the endpoints.

## 6 PDE Examples

In this section we explicitly evolve several test initial value problems using spectral methods as described in § 5. First, we examine the one-dimensional wave equation with Dirichlet and Neumann boundary conditions, and compare our results with the known behavior of such systems. We then explore the Kuramoto-Sivashinsky and complex Ginzburg-Landau equations, and compare our calculations with published results.

### 6.1 Wave equation

The one-dimensional wave equation on a finite domain is given by

$$\frac{d^2u}{dt^2} = c^2 \frac{d^2u}{dx^2} \quad (145)$$

where  $c$  is the wave propagation speed. To integrate this system with a Runge-Kutta method, we write it as the first order system

$$\frac{du}{dt} = v \quad (146)$$

$$\frac{dv}{dt} = c^2 \frac{d^2u}{dx^2} \quad (147)$$

We examine the equation over the domain  $[0, 1]$  with  $c = 1$ , and take a right-traveling pulse as our initial condition:

$$u_{\text{in}} = \exp \left[ \left( \frac{x - 0.5}{0.1} \right)^2 \right] \quad (148)$$

$$v_{\text{in}} = c \frac{du_{\text{in}}}{dx} \quad (149)$$

Using the extrema grid with 128 points, we integrated up to time  $t = 4$  using the 4-th and 5-th order Cash-Karp embedded Runge-Kutta algorithm, with an error tolerance  $\tau = 10^{-3}$ . Space-time diagrams for simulations with double homogeneous Dirichlet conditions (modeling a fixed string) and double homogeneous Neumann conditions are shown in Figure 13. The results agree with the expected analytical solutions that can be constructed using the method of images: in the Dirichlet case, the pulse reflects off of the boundaries with a change of sign, while in the Neumann case it piles up at the boundary and recoils with the same sign.

The same calculations were repeated after setting  $c = 1/2$  on the intervals  $[0, 0.3]$  and  $[0.7, 1.0]$ . The resulting space-time diagrams for Dirichlet and Neumann boundary conditions are shown in Figure 14. The change in wave speed and amplitude as the pulse crosses the interfaces are apparent, as are reflections off the interface.

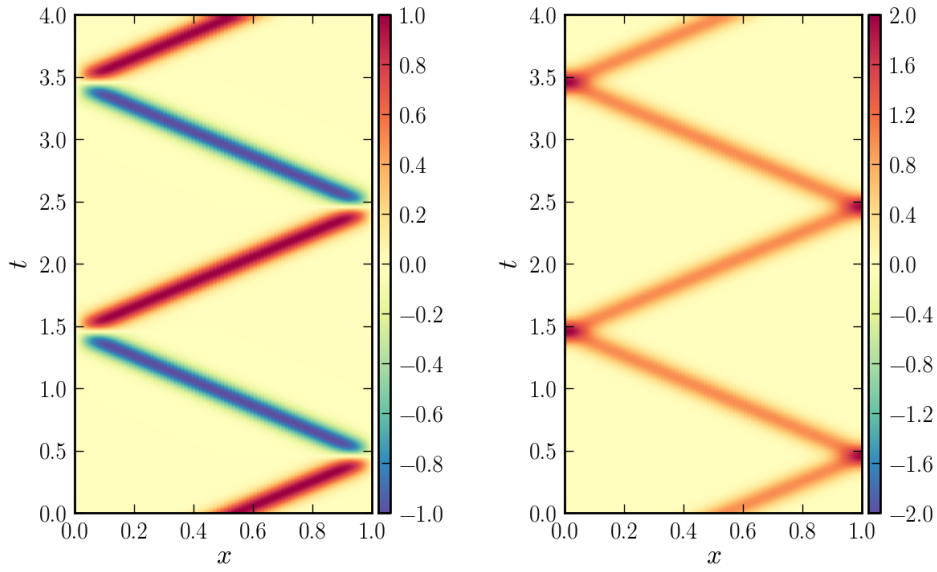


Figure 13: Wave equation with homogeneous Dirichlet (left) and homogeneous Neumann (right) boundary conditions, as computed on a 128-point Chebyshev extrema grid with a right-traveling Gaussian pulse initial condition.

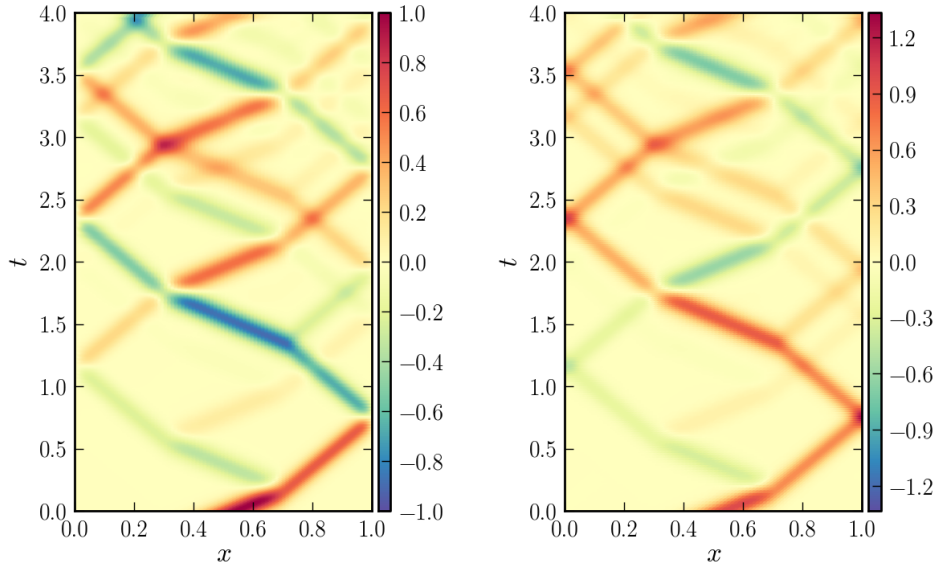


Figure 14: Wave equation with homogeneous Dirichlet (left) and homogeneous Neumann (right) boundary conditions with a slower wave speed in the outer regions, as computed on a 128-point Chebyshev extrema grid with a right-traveling Gaussian pulse initial condition.

The Dirichlet run was repeated with 256 points, and a narrower pulse. The state at  $t = 0.4$  is plotted in Figure 15, when the first reflection has returned to the center of the interval. The peak values of the reflected and transmitted pulses are  $-0.3362$  and  $0.6659$ , respectively, in agreement with the expected values of  $-1/3$  and  $2/3$  from the Fresnel equations to  $\mathcal{O}(10^{-3})$ .

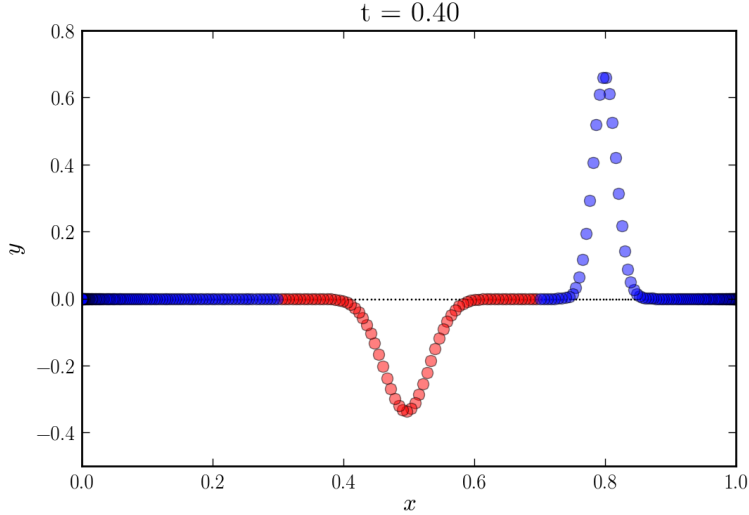


Figure 15: Solution after the initial right-traveling Gaussian pulse reflects off the interface at  $x = 0.7$ , as computed with 256 points. The reflected pulse at  $x = 0.5$  is traveling left and the transmitted pulse at  $x = 0.8$  is traveling right.  $c = 1/2$  in the blue regions, and  $c = 1$  in the red region.

## 6.2 Kuramoto-Sivashinsky equation

The generalized Kuramoto-Sivashinsky equation on a domain of length  $L$  is given by

$$\frac{du}{dt} + \lambda_1 \frac{d^4u}{dx^4} + \lambda_2 \frac{d^2u}{dx^2} + \lambda_3 u \frac{du}{dx} = 0 \quad (150)$$

The equation was originally derived as a model for phase turbulence in reaction-diffusion equations and to study the stability of a planar flame front. It also serves as a model for a variety of cellular instabilities, including Alfvén drift waves and thin flows down inclined planes (Liu and Krstić, 2001).

We can non-dimensionalize the equation by rescaling  $u$  by  $U$ ,  $t$  by  $T$ , and  $x$  by  $L$ ; the resulting equation is

$$\frac{du}{dt} + \alpha_1 \frac{d^4u}{dx^4} + \alpha_2 \frac{d^2u}{dx^2} + \alpha_3 u \frac{du}{dx} = 0 \quad (151)$$

on the domain  $[0, 1]$ , with

$$\alpha_1 = \frac{\lambda_1 T}{L^4} \quad (152)$$

$$\alpha_2 = \frac{\lambda_2 T}{L^2} \quad (153)$$

$$\alpha_3 = \frac{\lambda_3 UT}{L} \quad (154)$$

Hyman and Nicolaenko (1986) systematically studied the transition to chaos in the integral form of the equation

$$\frac{dw}{dt} + 4 \frac{d^4w}{dx^4} + \alpha \left[ \frac{d^2w}{dx^2} + \frac{1}{2} \left( \frac{dw}{dx} \right)^2 \right] = 0 \quad (155)$$

by varying  $\alpha$  between 0 and 120, with periodic boundary conditions on the interval  $[0, 2\pi]$ .

Choosing our scalings as  $L = 2\pi$ ,  $T = L^4/4$ , and  $U = L/(\alpha T)$ , we reproduce their configuration (up to the boundary conditions) by setting  $\alpha_1 = 1$ ,  $\alpha_2 = \alpha\pi^2$ , and  $\alpha_3 = 1$ . Instead of periodic boundary conditions, we take homogeneous Dirichlet and Neumann boundary conditions at both endpoints and examine the resulting dynamics.

Using 20-point Kosloff grids with  $\alpha = \cos(1/2)$  and the 4/5 Cash-Karp integrator with a tolerance of  $\tau = 1$ , we performed 25 simulations with  $\alpha$  ranging from 0 to 50, starting from the initial condition

$$u_{\text{in}} = \frac{1}{U} \sin(\pi x)^2 \quad (156)$$

The following table contains a comparison of our preliminary results for the solution behavior in this regime with those reported by [Hyman and Nicolaenko](#) using periodic boundary conditions. Due in part to the harsh timestep limitations on high-order explicit Chebyshev methods, our resolution and error tolerances were much weaker than the ones used to construct their solutions.

Attracting solution manifolds for the Kuramoto-Sivashinsky equation Comparison with Fourier-based periodic solutions of <a href="#">Hyman and Nicolaenko (1986)</a> (Sampling uncertainty indicated in parentheses)		
Dirichlet BC	Behavior	Periodic BC
$0 \leq \alpha \leq 4(1)$	Global attractor: 0	$0 \leq \alpha \leq 4$
$4(1) \leq \alpha \leq 24.5(0.5)$	Global attractor: essentially $\sin(2\pi x)$	$4 \leq \alpha \leq 17.3$
$24.5(0.5) \leq \alpha \leq 28.5(0.5)$	Periodic orbit $\sin(2\pi x)$	$17.3 \leq \alpha \leq 19$
$28.5(0.5) \leq \alpha \leq 34(1)$	Unstable bimodal fixed point	$19 \leq \alpha \leq 22.5$
$34(1) \leq \alpha \leq 44(1)$	Global attractor: essentially $\sin(4\pi x)$	$22.5 \leq \alpha \leq 43$
$44(1) \leq \alpha \leq 49+$	Oscillatory & chaotic orbits	$43 \leq \alpha \leq 54$

Representative space-time diagrams are also provided in [Figure 16](#). A more detailed study would certainly be feasible with further optimization of our code and increased computing time.

### 6.3 Complex Ginzburg-Landau equation

The complex Ginzburg-Landau equation (CGLE) is a second-order partial differential equation that can be used to model a very wide range of nonlinear dynamical systems. The equation describes the evolution of the complex wave amplitude  $A$ :

$$\frac{dA}{dt} = \mu A + s \frac{dA}{dx} + (1 + ib) \frac{d^2 A}{dx^2} - (1 + ic) |A|^2 A, \quad 0 \leq x \leq L \quad (157)$$

The CGLE is often studied in a periodic geometry where the group velocity term  $S \frac{dA}{dx}$  can be removed by to Galilean transformation. [Nana et al. \(2009\)](#), however, investigate the CGLE in a finite geometry with homogeneous Dirichlet boundary conditions, a form applicable to a variety of bounded systems. [Nana et al.](#) used a finite-difference scheme to evolve a pulse-like initial condition

$$u_{\text{in}} = A_0 \frac{(1 + i)}{\cosh(\gamma(x - L/2))} \quad (158)$$

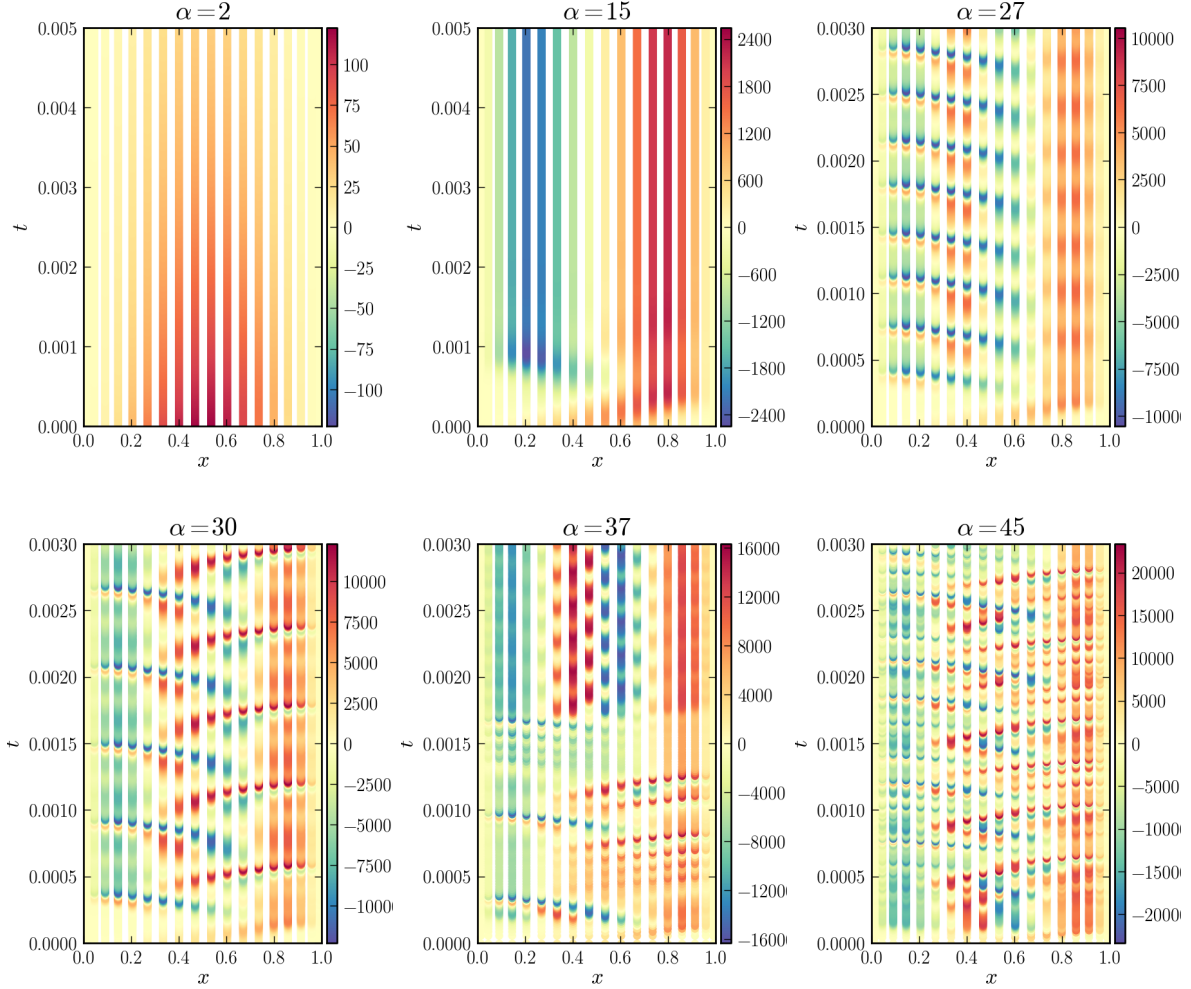


Figure 16: Solutions of the Kuramoto-Sivashinsky equation for representative values of  $\alpha$ , as computed on a 20-point Kosloff grid.

with amplitude  $A_0 = 0.01$  and  $\gamma = 100$ , while varying  $\mu$ ,  $s$ ,  $b$ ,  $c$ , and  $L$ . We will reproduce two of their results.

We begin by rewriting the CGLE as a coupled system for the real and imaginary parts of  $A$ . Letting  $A = u + iv$ , the resulting system is

$$\frac{du}{dt} = \mu u + s \frac{du}{dx} + \frac{d^2u}{dx^2} - b \frac{d^2v}{dx^2} - (u^2 + v^2)(u - cv) \quad (159)$$

$$\frac{dv}{dt} = \mu v + s \frac{dv}{dx} + \frac{d^2v}{dx^2} + b \frac{d^2u}{dx^2} - (u^2 + v^2)(v + cu) \quad (160)$$

$$u(0) = u(L) = v(0) = v(L) = 0 \quad (161)$$

[Nana et al.](#) describe the results of a simulation using  $\mu = 0.15$ ,  $s = 0.5$ ,  $b = 0.5$ ,  $c = -3.65$ , and  $L = 60$ , where the size of the non-linear dispersion coefficient  $c$  leads to the emergence of secondary structures near  $x = 0$  and on top of an absolutely unstable global mode. We used the same parameters with a 64-point Chebyshev representation on the Kosloff grid with  $\alpha = \cos(1/2)$ , and the 4/5 Cash-Karp integrator with error tolerance  $\tau = 10^{-6}$ . Our results are displayed in Figure 17; the described structure

is clearly visible in the amplitude plot.

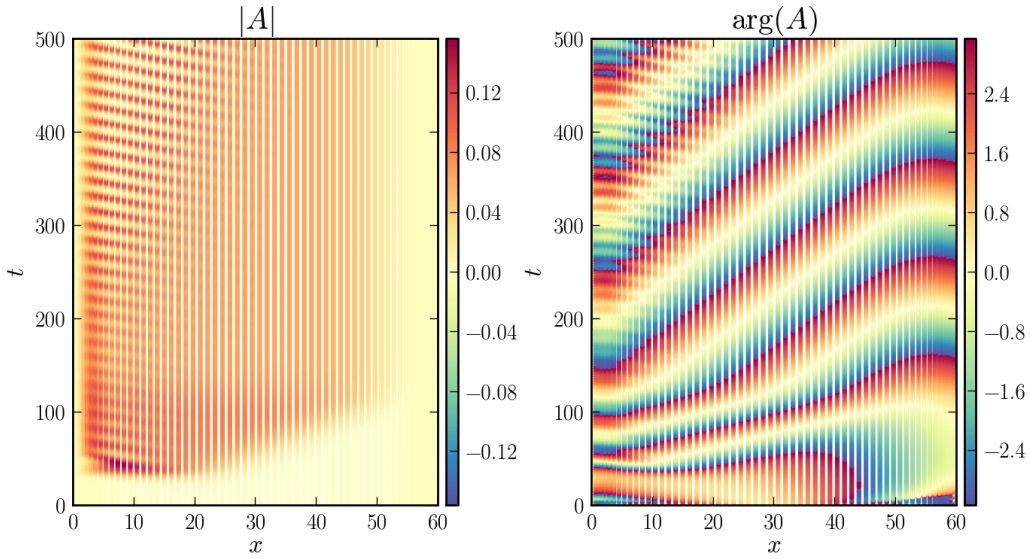


Figure 17: Amplitude and phase space-time diagrams showing secondary structures forming on top of an unstable global mode in the complex Ginzburg-Landau equation. The simulation used a 64-point Kosloff grid with  $\alpha = \cos(1/2)$ .

For small group velocities  $s$  and large length scales  $L$ , [Nana et al.](#) report a regime of spatial-temporal intermittency referred to as “hole-defect chaos” where amplitude depressions separate patches of chaotically interacting plane waves. We use their parameters  $s = 0.05$ ,  $\mu = 1$ ,  $b = 0.5$ , and  $c = -1.76$ , but shorten the domain from  $L = 600$  to  $L = 200$ , and resolve it with 200 grid points. Our results are displayed in Figure 18.

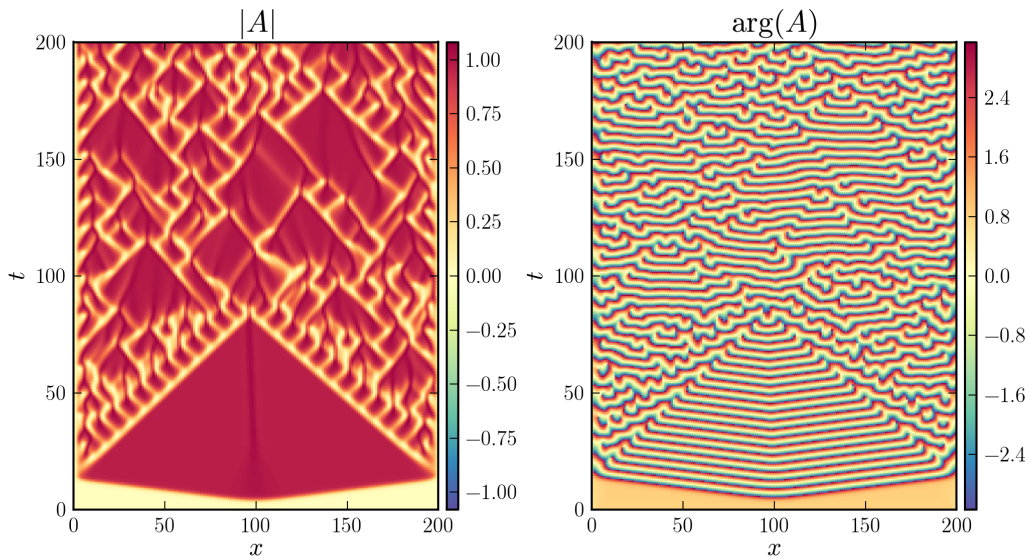


Figure 18: Amplitude and phase space-time diagrams depicting hole-defect chaos in the complex Ginzburg-Landau equation. The simulation used a 200-point Kosloff grid with  $\alpha = \cos(1/2)$ .

## 7 Conclusion

We have covered the basic theory and a variety of examples involving the use of Chebyshev spectral methods to numerically solve differential equations. The algorithms discussed in § 3 can be used to solve general linear ordinary differential equations with spatially varying coefficients, both in boundary value and eigenvalue form, and were verified with two recent results from the astrophysical fluids literature.

The methods discussed in § 5 can be used to explicitly evolve non-linear initial value problems with one space and one time dimension. While utilizing the remapped Kosloff grid improved the timestepping restrictions in our test problems, moving to an implicit time integration scheme would likely prove extremely beneficial by maintaining stability with much larger time steps. Such an improvement could make thoroughly exploring the solution manifolds of the Kuramoto-Sivashinsky equation with Dirichlet boundary conditions substantially more feasible.

## References

- John P Boyd. *Chebyshev and Fourier Spectral Methods*. Dover, 2nd edition, 2000.
- James M Hyman and Basil Nicolaenko. The Kuramoto-Sivashinsky Equation: A Bridge Between PDE's and Dynamical Systems. *Physica*, 18D:113–126, 1986.
- Dan Kosloff and Hillel Tal-Ezer. A modified Chebyshev pseudospectral method with an  $O(N-1)$  time step restriction. *Journal of Computational Physics*, 104(2):457–469, 1993.
- Henrik N. Latter and Matthew W. Kunz. The HBI in a quasi-global model of the intracluster medium. *Monthly Notices of the Royal Astronomical Society*, 423(2):1964–1972, June 2012.
- Henrik N. Latter, Sebastien Fromang, and Oliver Gressel. MRI channel flows in vertically stratified models of accretion discs. *Monthly Notices of the Royal Astronomical Society*, 406:848–862, May 2010.
- Wei-Jiu Liu and Miroslav Krstic. Stability Enhancement by Boundary Control in the Kuramoto-Sivashinsky Equation. *Nonlinear Analysis*, 43(485-507), 2001.
- Laurent Nana, Alexander B. Ezersky, and Innocent Mutabazi. Secondary structures in a one-dimensional complex Ginzburg-Landau equation with homogeneous boundary conditions. *Proceedings of the Royal Society A: Mathematical, Physical and Engineering Sciences*, 465(2107):2251–2265, April 2009.
- Jian-Ping Wang, Yoshiaki Nakamura, and Michiru Yasuhara. Global Coefficient Adjustment Method for Neumann Condition in Explicit Chebyshev Collocation Method and Its Application to Compressible Navier-Stokes Equations. *Journal of Computational Physics*, 107:160–175, 1993.